Physics in Medicine & Biology

IPEM Institute of Physics and Engineering in Medicine

PAPER

Implementation and validation of time-of-flight PET image reconstruction module for listmode and sinogram projection data in the STIR library

Nikos Efthimiou[1,2,3], Elise Emond[2], Palak Wadhwa[3,4], Christopher Cawthorne[1], Charalampos Tsoumpas[3,4] and Kris Thielemans[2]

[1] PET Research Centre, Faculty of Health Sciences, University of Hull, Hull, United Kingdom
[2] Institute of Nuclear Medicine, University College London, United Kingdom
[3] Department of Biomedical Imaging Science, School of Medicine, University of Leeds, Leeds, United Kingdom
[4] Invicro, Hammersmith Hospital, London, United Kingdom

E-mail: n.efthymiou@hull.ac.uk

Abstract

In this paper, we describe the implementation of support for time-of-flight (TOF) positron emission tomography (PET) for both listmode and sinogram data in the open source software for tomographic image reconstruction (STIR). We provide validation and performance characterization using simulated data from the open source GATE Monte Carlo toolbox, with TOF configurations spanning from 81.2 to 209.6 ps. The coincidence detector resolution was corrected for the timing resolution deterioration due to the contribution of the crystal length. Comparison between the reconstruction of listmode and sinogram data demonstrated good agreement in both TOF and non-TOF cases in terms of relative absolute error. To reduce the reconstruction time, we assessed the truncation of the TOF kernel along lines-of-response (LOR). Rejection of LOR elements beyond four times the TOF standard deviation provides significant acceleration of $\approx 45\%$ without compromising the image quality. Further narrowing of the kernel can provide extra time reduction but with the gradual introduction of error in the reconstructed images. As expected, TOF reconstruction performs better than non-TOF in terms of both contrast-recovery-coefficient (CRC) and signal-to-noise ratio (SNR). CRC achieves convergence faster with TOF, at lower noise levels. SNR with TOF was superior for early iterations, but with quick deterioration. Higher timing resolution further improved reconstruction performance, while TOF bin mashing was shown to have only a small impact on reconstructed images.

1. Introduction

Until relatively recently, PET detectors on commercially available PET scanners had a timing resolution of a few nanoseconds. Therefore, data acquired by the scanner provided the position of the emitting atom to within a line across the two detectors. Time-of-flight (TOF) capable scanners measure the temporal difference in the γ-photon detection with sufficient accuracy to provide an indirect measurement of the most likely location of the annihilation, thereby increasing the signal-to-noise ratio (SNR) (Nemallapudi *et al* 2015, Dujardin *et al* 2018).

Although early experimental PET scanners had TOF capabilities by using barium fluoride (BaF) scintillators (Laval *et al* 1983), these crystals had low stopping-power and the photo-detector technology and speed of the acquisition electronics were not developed sufficiently for stable operation.

In the early 2000s, the introduction of lutetium oxyorthosilicate (LSO) and lutetium-yttrium oxyorthosilicate (LYSO) scintillation crystals with high light output, good stopping power and fast responses revitalized TOF as an area of interest (Melcher and Schweitzer 1992, Moses and Derenzo 1999, Popescu *et al* 2004).

The first generation TOF-capable clinical scanners had a coincidence timing resolution of around 600 ps (Moses 2003), with recent systems using silicon photomulipliers (SiPM) detectors achieving 250–350 ps (Surti *et al* 2007, Grant *et al* 2016).

Much of the mathematical background for TOF reconstruction was presented by Snyder *et al* (1981), Tomitani (1981) and Snyder and Politte (1983), who envisaged efficient reconstruction where measurements would be made with an arbitrary timing accuracy and the radioactivity distribution could be estimated by histograms derived with no more than a scaling to account for the speed of the 511 keV γ-photons (Mullani *et al* 1981, Snyder 1981, Wong *et al* 1983).

The early publications focused on the benefits of using signal-to-noise ratio (SNR) gain as a metric of sensitivity (Mullani *et al* 1984, Wagner and Brown 1985).

Conti *et al* (2005) presented the benefits of TOF for an LSO-based PET scanner. By comparing noise-contrast curves, they demonstrated that TOF reconstructions converge faster and achieve better contrast recovery (CR) than non-TOF reconstructions. In addition, this study highlighted the issue of coarse time binning, which may contribute to the degradation of Poisson statistics.

Thoen *et al* (2013) used listmode TOF reconstruction of Monte Carlo simulated data to determine the effects of different PET detector timing parameters on the performance of simultaneous PET-MR systems. They studied the effect of TOF resolution, transverse pixel size and depth of interaction correction on image quality, in terms of spatial resolution, contrast recovery and SNR and the study concluded that the image quality can be significantly improved by reducing the transverse pixel size and improving the TOF resolution.

Brunner and Schaart (2017), reported that the cost-efficient bismuth germanate (BGO) crystals, used mostly in older generation scanners, may be capable of providing TOF information, too.

Commercial TOF-capable systems are provided with a proprietary closed source toolkit for acquiring and reconstructing data. However, there is a strong need for independent, open source software libraries to support the development of prototype scanners (Moskal *et al* 2016) or research in medical imaging (Martins *et al* 2005, Ahn *et al* 2018, Berg and Cherry 2018). Independent reconstruction software packages that support TOF reconstruction include MOLAR (Johnson *et al* 2004, Jin *et al* 2013), QETIR (Thoen *et al* 2013, Kolstein and Chmeissani 2016) and more recently CASToR2 (Merlin *et al* 2018).

The software for tomographic image reconstruction (STIR) library is the oldest open source software in the field, originating back to the PARAPET project (1997–1999), a European Union ESPRIT project on parallel 3D PET reconstruction algorithms. The library's source code was first released in June 2000 and a second release was made publicly available in 2009 (Thielemans *et al* 2006, 2012). The current stable version of the library is v3.0.

In this paper we present the introduction of TOF (projection and listmode) reconstruction in the STIR library and the corresponding validation and performance evaluation through GATE Monte Carlo (MC) simulations (Jan *et al* 2004). It is for the first time, a freely distributed software is being used to investigate of the benefits of the TOF reconstruction. The source code will be made available as an open source in the forthcoming release of the library.

2. Image reconstruction with time of flight

Tomographic image reconstruction tries to estimate volumetric images of the radiopharmaceutical distribution, using as input data acquired by the scanner. Iterative methods try to fit the data to a statistical model of the scanner which considers the underlying physics (Kinahan *et al* 2004). Excluding background events, the forward model of emission tomography (ET) can be represented by the linear equation:

$$\bar{g} = Pf \tag{1}$$

where $\bar{g}$ represents a vector of the projection data expected to be measured, f represents the unknown underlying radiotracer distribution image vector and P is the system matrix which represents the scanner's geometry and physical imaging processes.

Let each element p_{ij} of the matrix P represent the mean contribution of voxel j to projection element bin i. In the simplest case of solely geometrical contributions, the weights in P can be approximated by the intersection of the volumetric elements (voxels) to a line of response (LOR), specific for each bin or a detector pair. For this calculation, STIR normally uses a variation of Siddon's ray tracing algorithm (Siddon 1985), optionally with multiple rays per detector pair (Jacobson *et al* 2000), although other system models are equally supported, too. All voxels which do not intersect with the LOR are immediately excluded.

TOF-capable scanners have the capacity to record the difference in arrival times between the two γ-photons. This narrows the uncertainty of the origin of the annihilation along the LOR. When the detection time difference is taken into account the equation (1) can be formulated as:
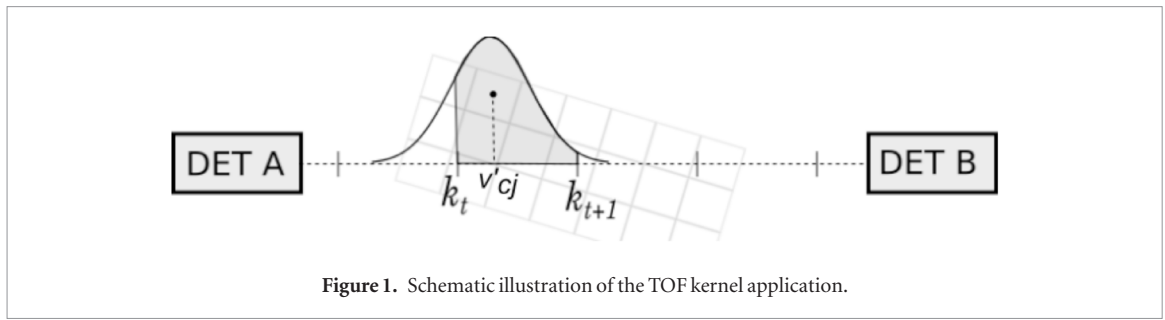
Figure 1. Schematic illustration of the TOF kernel application.

$$\bar{g}_{it} = \sum_j p_{it;j} f_j \tag{2}$$

where t is the index of the TOF bin.

If the voxel size is much smaller than the uncertainty in location due to the timing resolution, the system matrix can be computed, in good approximation, as:

$$p_{it;j} = p_{ij} K_{itj} \tag{3}$$

where K_{itj} is the time-spread-function (TSF) for the tth TOF bin.

2.1. Image reconstruction

STIR supports a wide range of algorithms for the determination of the maximum likelihood estimate (MLE), including ordered subsets expectation maximization (OSEM), median root prior (MRP) and quadratic prior (QP) Bayesian one step late methods (Erdogan and Fessler 1999, Green *et al* 2010), and the ordered subsets separable paraboloidal surrogates algorithm (Ahn and Fessler 2003). However, for the scope of this paper, only maximum likelihood expectation maximization (MLEM) was used (Shepp and Vardi 1982) as it is the simplest option, and is guaranteed to converge (even slowly) to a solution. However, due to the modular nature of STIR, all iterative algorithms are now support TOF.

Jacobson *et al* (2000) presented the MLEM version for projection data in the STIR library, however, a newly introduced listmode MLEM (LM-MLEM) (Barrett *et al* 1997), is included within this major upgrade of the library and is formulated as follows:

$$\lambda_j^{(n+1)} = \frac{\lambda_j^{(n)}}{S_j} \sum_{\epsilon \in E_\epsilon} \frac{p_{d_\epsilon t_\epsilon;j}}{\sum_{j'} p_{d_\epsilon t_\epsilon;j'} \lambda_{j'}^{(n)}} \tag{4}$$

where $\lambda^{(n)}$ is the estimated image at the nth iteration, $\epsilon \in E_\epsilon$ are the events in the listmode file, d_ϵ is the detector pair for event ϵ and t_ϵ is its TOF bin. S_j is the backprojection of the detection efficiency for all LORs, which provides the sensitivity image, given as:

$$S_j = \sum_d^D p_{dj} \frac{1}{N_d A_d} \tag{5}$$

with D the set of all detector pairs, N_d is the normalization, A_d the attenuation correction factor. The absence of a sum over the TOF bins in the sensitivity image calculation is a consequence of equation (3).
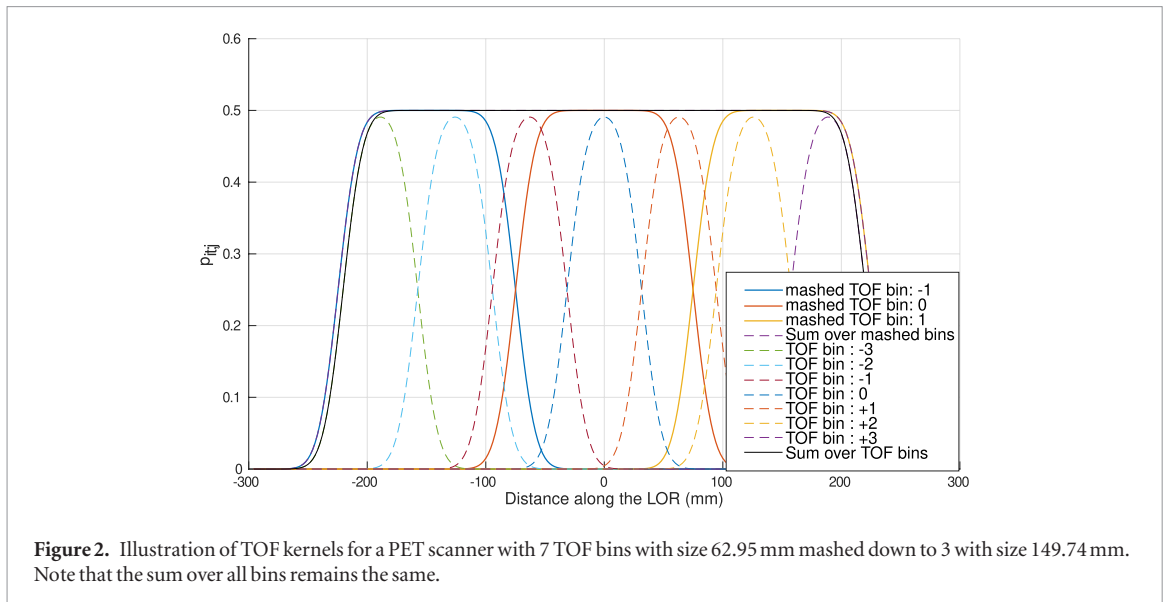
2.2. TOF kernel application

For the TOF kernel model we will assume, as common in the literature, that the PET scanner measures the difference in arrival times with the uncertainty that can be modelled with a normal distribution.

As current PET scanners store the data using discrete TOF information, this distribution needs to be integrated over the TOF bins. In addition, this uncertainty in arrival time needs to be converted to spatial information. Figure 1 illustrates the application of the TOF kernel.

For each voxel j in the non-TOF row, let v'_{cj} be the projection of the Cartesian coordinates of each voxel's center on the vector connecting the two detectors $\vec{AB}$.

For a given projection of the annihilation position along the LOR (v'_{cj}), the position corresponding to the detected timing difference follows a Normal distribution (μ, σ), where μ is v'_{cj} and σ is the standard deviation (SD) of the timing resolution of the scanner (Mehranian *et al* 2016).

The probability of detection in a certain TOF bin can then be computed using its cumulative distribution function (cdf). As a result, the timing dependent probability K_{itj} is given by:

Figure 2. Illustration of TOF kernels for a PET scanner with 7 TOF bins with size 62.95 mm mashed down to 3 with size 149.74 mm. Note that the sum over all bins remains the same.

$$
\begin{aligned}
K_{itj} &= \mathrm{cdf}(k_{t+1} - v'_{cj}) - \mathrm{cdf}(k_t - v'_{cj}) \\
&= \frac{1}{2}\left(\mathrm{erf}\left(\frac{k_{t+1} - v'_{cj}}{\sigma\sqrt{2}}\right) - \mathrm{erf}\left(\frac{k_t - v'_{cj}}{\sigma\sqrt{2}}\right)\right)
\end{aligned}
\tag{6}
$$

where we expressed the distance of the integration boundaries $[k_t, k_{t+1})$ of the tth TOF bin, from the v'_{cj} point in multiples of the timing kernel's SD.

Some PET scanners have the capability to use TOF *mashing*, where a number of TOF bins are combined by spacing out the integration boundaries. This process leads to smaller data sizes. Figure 2 illustrates the TOF kernel when using TOF mashing, for a single ray. The initial setup had 7 TOF bins with integration boundaries every 62.95 mm. Subsequently, a mashing factor of 3 was applied to reduce the number of TOF bins to 3 with integration size of 149.74 mm. Please note that the *sum over all bins* in both cases are the same. This confirms that equation (6) is implemented properly.

3. Materials and methods

3.1. Monte Carlo simulations

3.1.1. Scanner geometry and coincidence timing resolution

The geometry of a cylindrical PET scanner was simulated using the GATE simulation toolkit (v.7.2) (Jan *et al* 2004).

The scanner had 24 rings with 666 detectors per rings. No gaps were considered. The cylindrical PET hierarchy was used with, with 666 Rsectors, each one having one row of 24 crystals. The reason behind this arrangement was to the scanner's geometry as close as possible to a cylinder, without gaps, as STIR does not support models of blocked geometries.

The inner ring radius was 424.5 mm and the total axial length 110.0 mm. The crystals were made of LSO:Ce (Melcher and Schweitzer 1992) with size $4 \times 4 \times 20$ mm^3. The energy resolution of the system was set to 11.7% and the applied energy window was 435–650 keV. The coincidence time window was set to 3 ns.

The number of TOF bins was set to 2999 with integration size 0.149 mm. In order to have a centered zero index bin, the number of TOF bins was kept odd. Detector dead-time was not considered. Three coincidence timing resolutions were considered: 50.0, 100.0 and 200.0 ps.

Post simulation, the detection time differences were sorted in histograms and fitted to a Gaussian function. After fitting the simulated data, the actual system's timing resolution (FWHM$_T$) values were found to be 81.2 ps, 118.4 ps and 209.6 ps, correspondingly. The difference between the expected and the actual FWHM$_T$ can be then explained by the photon transport spread (PTS), which contributes to the timing resolution deterioration (for more information, see appendix). The values found from the kernel fitting were those used for the TOF reconstruction.

For the sake of simplicity the three timing resolution will be labelled as TOF-80, TOF-120 and TOF-210, throughout the paper.
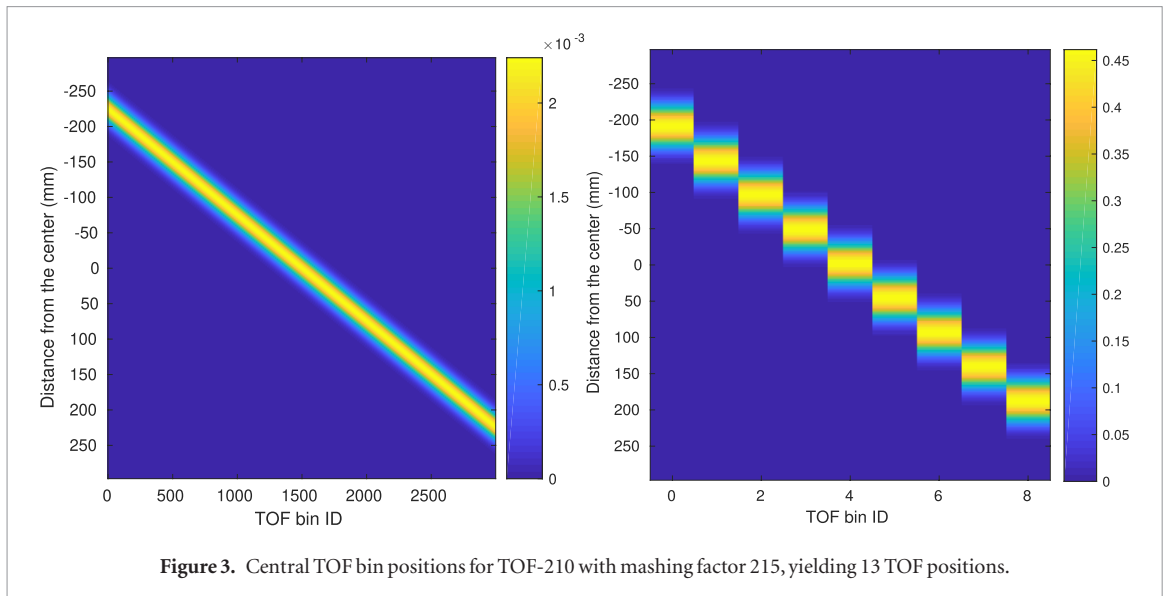
Figure 3. Central TOF bin positions for TOF-210 with mashing factor 215, yielding 13 TOF positions.

3.1.2. Simulated phantom

An acquisition of the NEMA IQ phantom was simulated (National Electrical Manufacturers Association 2012). The computational phantom had the exact same dimensions as the physical IQ phantom. Four radioactive, hot, spheres (radii 5, 6.5, 8.5 and 11 mm) and 2 cold spheres (radii 14 and 18.5 mm) were introduced. The spheres were placed at the radial distance of 114.4 mm from the centre of the phantom and were centered axially. At the center of the phantom a cold cylinder made of the material equivalent to lung tissue, was placed.

The activity ratio between the sources and the background was 4 : 1. Random and scattered photon events were excluded post simulation.

The sinogram dimensions were 333 views ×320 tangential positions and 27 segments.

3.2. Image reconstruction

The voxel size of the reconstructed images was $2 \times 2 \times 2.08$ mm^3 with $297 \times 297 \times 47$ voxels, in total. No post-reconstruction smoothing filters were applied to the images.

Attenuation correction factors were produced with an analytical simulation, of the phantom, having the appropriate linear attenuation values for 511 keV γ-photons, as found in NIST (Hubbell and Seltzer 1995).

Normalization factors were calculated using a component-based methodology (Pépin *et al* 2012, Efthimiou *et al* 2015). In brief, a cylindrical back-to-back source with diameter 400 mm, without an attenuating component was simulated with Monte Carlo for a long acquisition obtaining approximately 10×10^8 events. Fan sums were used, taking into consideration the axial and transaxial geometrical non-uniformity, crystal interleaving, detector efficiencies and block profiles.

3.3. Comparison between sinogram and listmode reconstruction

A GATE simulated dataset of approximately 10×10^6 counts was used for the comparison between the LM and projection reconstruction. The agreement between the two modes was validated for non-TOF and all TOF configurations.

The TOF data were histogrammed in sinograms with 13 TOF bins using timing mashing factor 215. The same timing mashing factor was applied in LM reconstruction. In figure 3 the central nine positions out of the 13 TOF positions for a single LOR, are illustrated.

The comparison was performed in terms of relative absolute error (*E*) using averaged images over 10 noise realizations.

3.3.1. Relative absolute error

The default image comparison tool (*compare_image*) provided in STIR quantifies the largest error and is calculated by the following formula:

$$E = \frac{max(|Y - X|)}{max(|Y|)},$$

(7)

where *Y* is the first image and *X* is the second to be compared.

3.4. TOF kernel truncation

The duration of the reconstruction process strongly depends on the size of the projection matrix row. With TOF, the truncation of the LOR at a specific distance from the center of the TOF bin is possible (Daube-Witherspoon *et al* 2007). An investigation for the potential introduction of error due to truncation on different distances from the center of the TOF bin was performed. The distances 1.4, 2.7, 3.0, 3.5 and 4σ, were considered. Listmode reconstruction, without TOF mashing, for approximately 11×10^6 events, was performed for 50 iterations.

For the purpose of this comparison, all reconstructions were performed on an Intel i7 Skylake 6700 K processor with 16 GB RAM and SSD drive, using a single thread. STIR provides the options of OPEN-MP and MPI (Thielemans *et al* 2015) but were not used in this instance.

3.5. Investigation of the performance of the time-of-flight reconstruction

3.5.1. ROI analysis

For each sphere the mean, standard deviation (SD) and coefficient of variation (CoV) were calculated using tools included in the STIR library. Circular regions of interest (ROIs) with the same radius as each source, were selected. The ROIs were drawn on the central slice, where the profile of the spheres was the largest. In our case, according to the alignment of the phantom and the scanner that slice was the 24th. Background ROIs of the same size as those used on the spheres were placed in the background area. The selected positions were non-symmetrical with respect to the center of the image. Twelve such background ROIs per slice for ± 2 slices from the central slice, for each source, were considered. All background ROIs were placed so that none was closer than 15 mm to any sphere (National Electrical Manufacturers Association 2012).

3.5.2. Contrast recovery coefficient

The average contrast recovery coefficient ($\overline{\mathrm{CRC}}_H$) for each hot sphere ($H$) was calculated over four noise realizations ($p \in P$) with $\approx 18 \times 10^6$ events each, using the formula (National Electrical Manufacturers Association 2012, Westerwoudt *et al* 2014):

$$\overline{\mathrm{CRC}}_{H,r} = \frac{1}{N_P} \sum^{P} \frac{\left(\frac{\mu_{H,r}}{\mu_{B,r}} - 1\right)}{\alpha - 1} \times 100\%, \tag{8}$$

where $\mu_{H,r}$ denotes the mean value of the of hot sphere's (H_r) ROI, $\mu_{B,r}$ denotes the mean background ROI value and $\alpha = 4$ which is the true activity ratio between the hot spheres and the background.

Respectively, in the case of the cold spheres C, r the $\overline{\mathrm{CRC}}_{C,r}$ was calculated by:

$$\overline{\mathrm{CRC}}_{C,r} = \frac{1}{N_P} \sum^{P} \left(1 - \frac{\mu_{C,r}}{\mu_{B,r}}\right). \tag{9}$$

The background viability was expressed as the coefficient of variation (CoV$_r$), calculated for each sphere with size r as:

$$\overline{\mathrm{CoV}}_r = \frac{1}{N_P} \sum^{P} \frac{\sigma_{B,r}}{\mu_{B,r}}. \tag{10}$$

3.5.3. Signal to noise ratio (SNR)

For the assessment of the SNR performance, four datasets with $\approx 18 \times 10^6$ events, were used. The SNR was calculated according to the formula (Westerwoudt *et al* 2014):

$$\overline{\mathrm{SNR}}_r = \frac{1}{N_P} \sum^{P} \frac{\mu_{H,r} - \frac{1}{N_B} \sum \mu_{B,r}}{\frac{1}{N_B} \sum \sigma_{B,r}}. \tag{11}$$

4. Results

4.1. Comparison between sinogram and listmode reconstruction

The sinogram and listmode reconstructions are in very good agreement for both TOF and non-TOF cases with E below 0.009% at 10th, 30th and 40th iteration for non-TOF, TOF-80, TOF-120 and TOF-210. The small differences were expected as STIR uses single precision calculations.

Further, investigation of the difference images at the 38th iteration do not demonstrate any striking local artifacts between the different regions (figure 4).
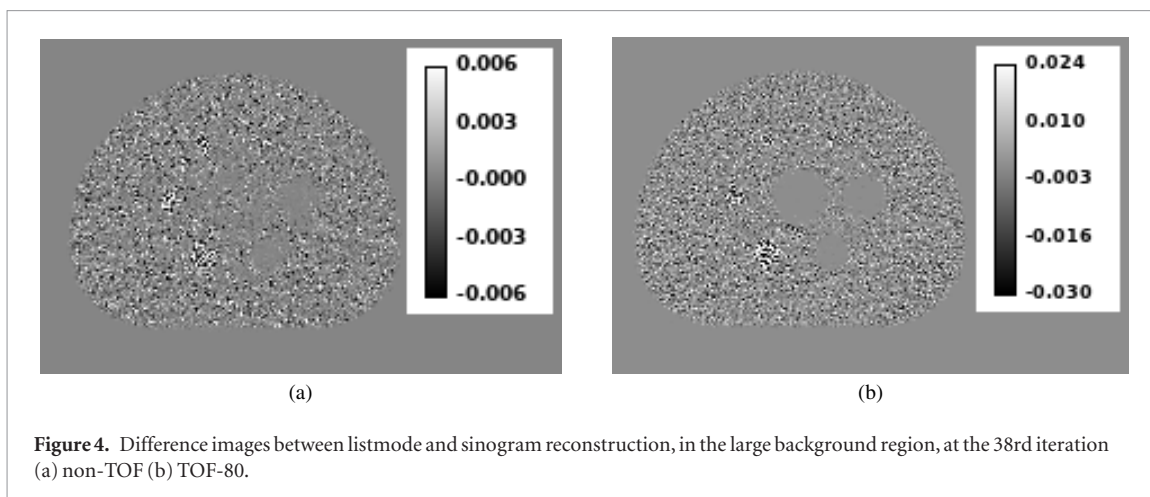
Figure 4. Difference images between listmode and sinogram reconstruction, in the large background region, at the 38rd iteration (a) non-TOF (b) TOF-80.
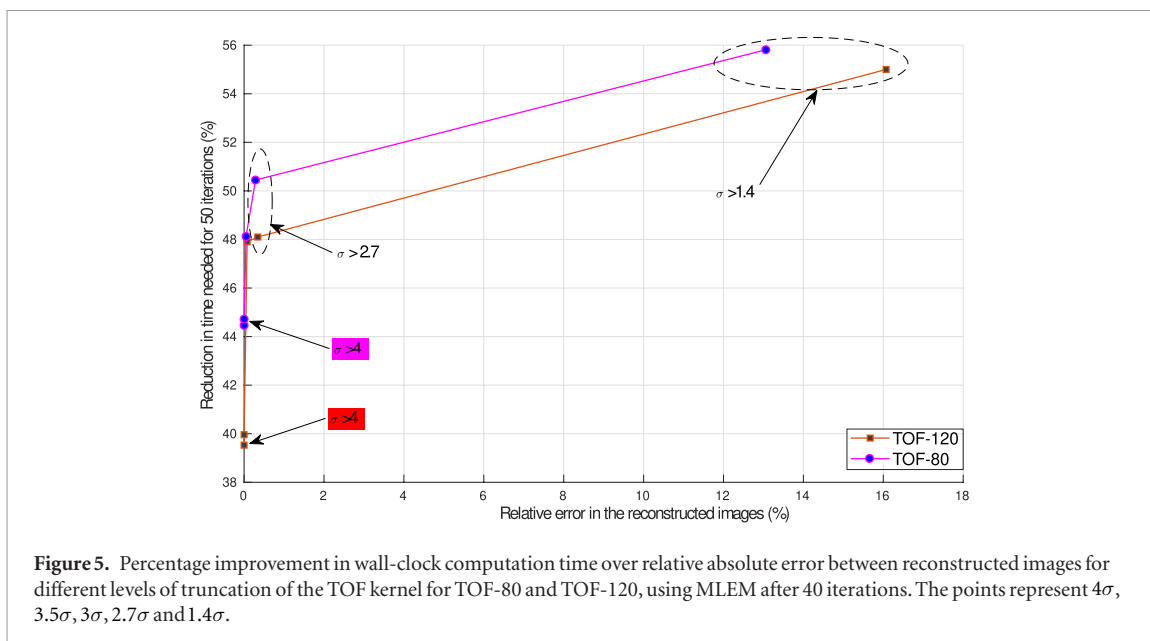

Figure 5. Percentage improvement in wall-clock computation time over relative absolute error between reconstructed images for different levels of truncation of the TOF kernel for TOF-80 and TOF-120, using MLEM after 40 iterations. The points represent 4σ, 3.5σ, 3σ, 2.7σ and 1.4σ.

4.2. TOF kernel truncation

Figure 5 illustrates the impact of different levels of LOR truncation in terms of (wall-clock) computation time and relative error in the reconstructed images for TOF-80 and TOF-120. As expected, TOF-80 which has the narrowest kernel demonstrated the largest reduction on their wall-clock computation time compared to TOF-120.

Reconstruction times were improved to $\approx 45\%$ when truncating 4.0σ with practically no measurable impact in the reconstructed image. The majority of the rejected voxels in each TOF position did not relate to that particular position, their probability was negligible, left over from the initial non-TOF LOR.

The cases 3.5σ and 3σ seemed to be equally appropriate alternative options for the NEMA phantom simulation and the statistics obtained in this simulation. We anticipate that this will vary with noise level and regularization. Further, truncation with 1.4σ offered an acceleration of up to 55% but with a significant impact of E of the images. The largest differences are located near the boundaries of the phantom and at locations of high contrast. Larger smooth areas were not affected to the same extent in most cases, although 1.4σ demonstrated a strong impact in all locations of the phantom.
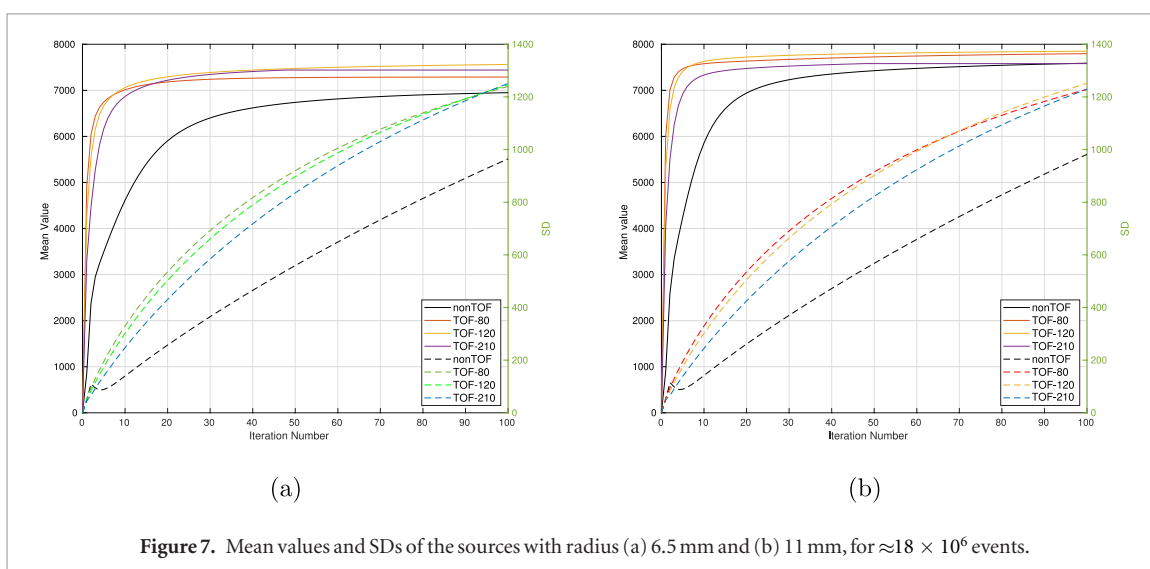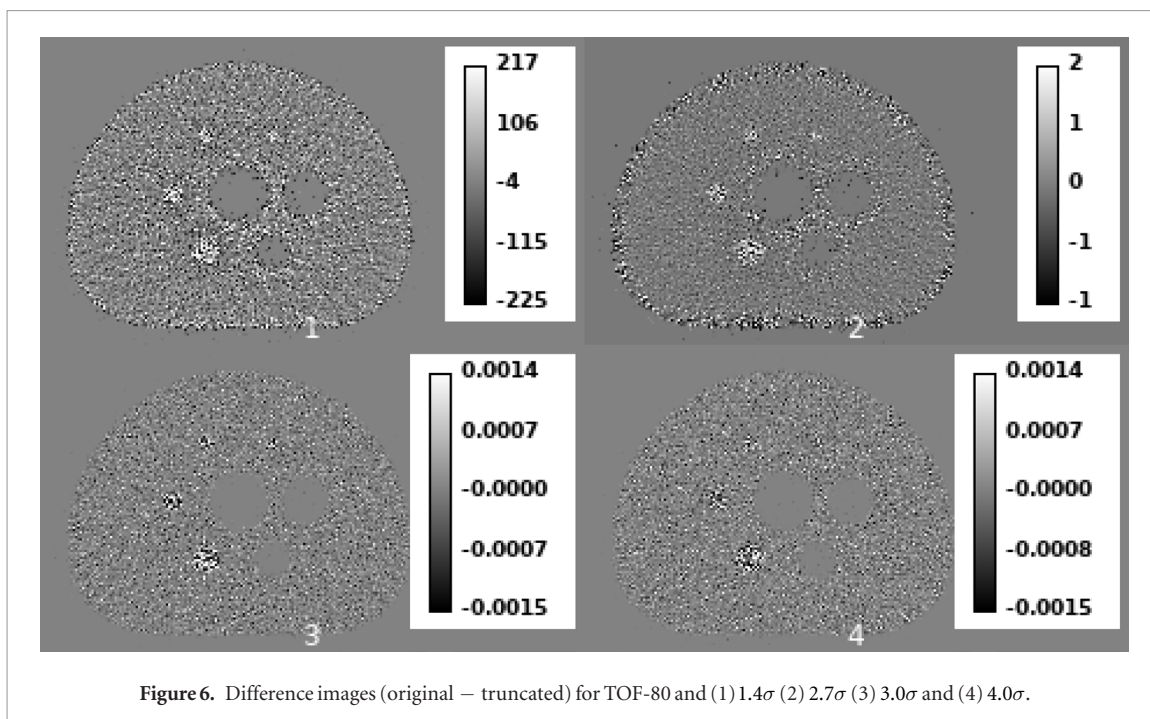
Figure 6 shows that there is a clear localization of the effect of truncation.

In the case of TOF-80, STIR was able to process 6050 events per second without truncation which with 4σ increase to 10 222. Non-TOF has a throughput of 17 037 events per second.

4.3. Mean values and SD

In figure 7 the mean value in the region of the two larger hot spheres and the background SD values, are shown. TOF converge much faster than non-TOF reconstruction.

For the largest hot sphere, $\mu_{H,4}$ converged to the approximately same values for all configurations (figure 7(b)), but the 6.5 mm sphere non-TOF reached a $\approx 9\%$ lower value.

Figure 6. Difference images (original − truncated) for TOF-80 and (1) 1.4σ (2) 2.7σ (3) 3.0σ and (4) 4.0σ.

    (a)   (b)

Figure 7. Mean values and SDs of the sources with radius (a) 6.5 mm and (b) 11 mm, for $\approx 18 \times 10^6$ events.

Worth noting that the mean values of the two sources are approximately the same with TOF reconstruction.

The background SD kept increasing throughout the range of iterations, significantly faster in the TOF cases than the non-TOF.

4.4. Contrast recovery coefficient

In figure 8 CRC over CoV for 100 iterations for the largest hot and cold spheres, is presented. Note that we did not iterate MLEM long enough to achieve convergence for nonTOF, but enough to demonstrate the benefits of TOF. Contrast recovery around 97% is achieved with high resolution TOF, while low resolution TOF and non-TOF reach a slightly lower value.

Smaller spheres recover to smaller values as 90% for the 8.5 mm sphere.

In all cases, high-resolution TOF performs better than low-resolution TOF and non-TOF. For example, for the 11 mm sphere, 95% recovery is reached after four iterations with a 16% noise level using TOF-80, while TOF-210 needs 17 iterations and achieves 24% noise.

The positive effect of TOF reconstruction is particularly evident in the cold spheres. Without TOF the recovery is significantly slower (figure 8(b)). Cold areas are known to be problematic to MLEM reconstruction.

Figure 9 shows example reconstructed images. For each configuration the iteration number was selected where the CRC of the largest hot sphere reached 95% of its maximum CRC. For non-TOF, TOF-80, TOF-120 and TOF-210 the 65th, 5th, 7th and 13th iterations were selected, respectively.
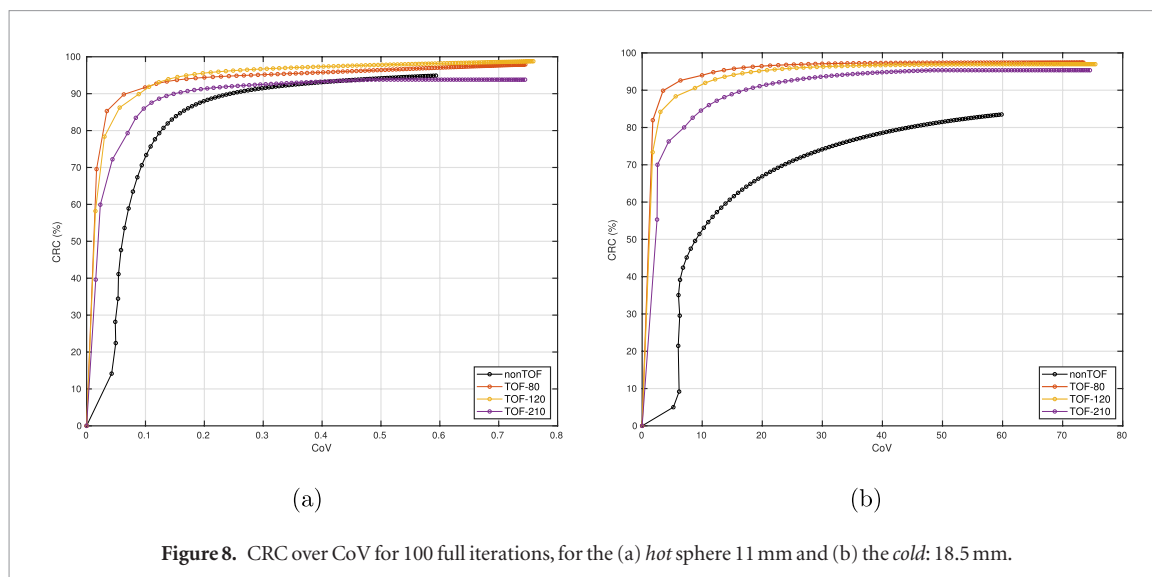
Figure 8. CRC over CoV for 100 full iterations, for the (a) *hot* sphere 11 mm and (b) the *cold*: 18.5 mm.

For the circular profiles it is evident that the non-TOF reconstruction has poorer noise characteristics. In addition, the cold sources have not reached value 0 in most cases as it converges slower than the hot sphere, which was used to select the iteration number. The smaller spheres, especially the 5 mm, have the lower contrast, but more effects contribute to that, as partial volume error.

CRC sees a minimal impact from TOF mashing. Using only 13 TOF positions to perform the reconstruction resulted in 2%–3% worse recovery, mainly for higher resolutions.

4.5. Signal to noise ratio

TOF reconstruction drastically improved the SNR at early iterations, as demonstrated for the two larger hot spheres, in figure 10.

However, at a certain iteration (in most cases before the 10th) the SNR of the TOF images got poorer than the non-TOF case. Finally, non-TOF and TOF reconstructed images reach to approximately similar SNR levels in the range of iterations we studied.

On early iterations, TOF mashing has a small impact on the SNR peak value about 5% or less. But quickly after few iterations the mashed and non-mashed SNRs are aligned.

5. Discussion

Development of the TOF feature in the STIR reconstruction toolbox is a major update. The majority of modern scanners have TOF capable detectors. In addition, LM reconstruction is favored nowadays, as the size of the stored data is growing due to the timing positions, larger scanner sizes and better angular sampling.

Similarly to other authors (Karp *et al* 2008, Conti *et al* 2013, Westerwoudt *et al* 2014, Suljic *et al* 2015, Surti 2015, Zhang *et al* 2018), we demonstrated that when using TOF, CRC converges faster. Comparison between different timing resolutions showed that the convergence speed is further improved when the scanner has better timing resolution. The benefits of TOF reconstruction are more evident in cold sources, which are a known issue in non-TOF MLEM reconstruction. The mean values per ROI, for the larger spheres convergence to approximately the same value (<5% variation) is achieved, which is a good indication of only minimal bias introduction, in the TOF system model (see below for further discussion).

In terms of SNR, TOF performs better at low iteration numbers, as the mean value of the source is significantly higher than in the non-TOF case. Almost when the maximum mean value is reached, the SD becomes the driving factor and SNR decreases faster for TOF compared to non-TOF reconstruction. Similar behavior has been demonstrated by other authors (Conti *et al* 2013, Westerwoudt *et al* 2014). In our case, we found that TOF does not actually provide improved SD values, but actually the benefits on the SNR come from the improved source mean value which rises faster. This behaviour is stronger for higher timing resolutions, which makes the need to stop MLEM at the proper iteration more critical.

Monte Carlo simulations in medical imaging research are used for a wide range of purposes, support for the reconstruction of such data is in high demand. Therefore an interface which supports the reconstruction of data produced in the GATE toolbox was developed. Using GATE simulations and fast timing resolution simulations, we observed the importance of the photon detection time spread. Otherwise underestimated TOF kernels will be used in the reconstruction. It is important to fit the TOF timing resolution to the observed timing of the coinci-
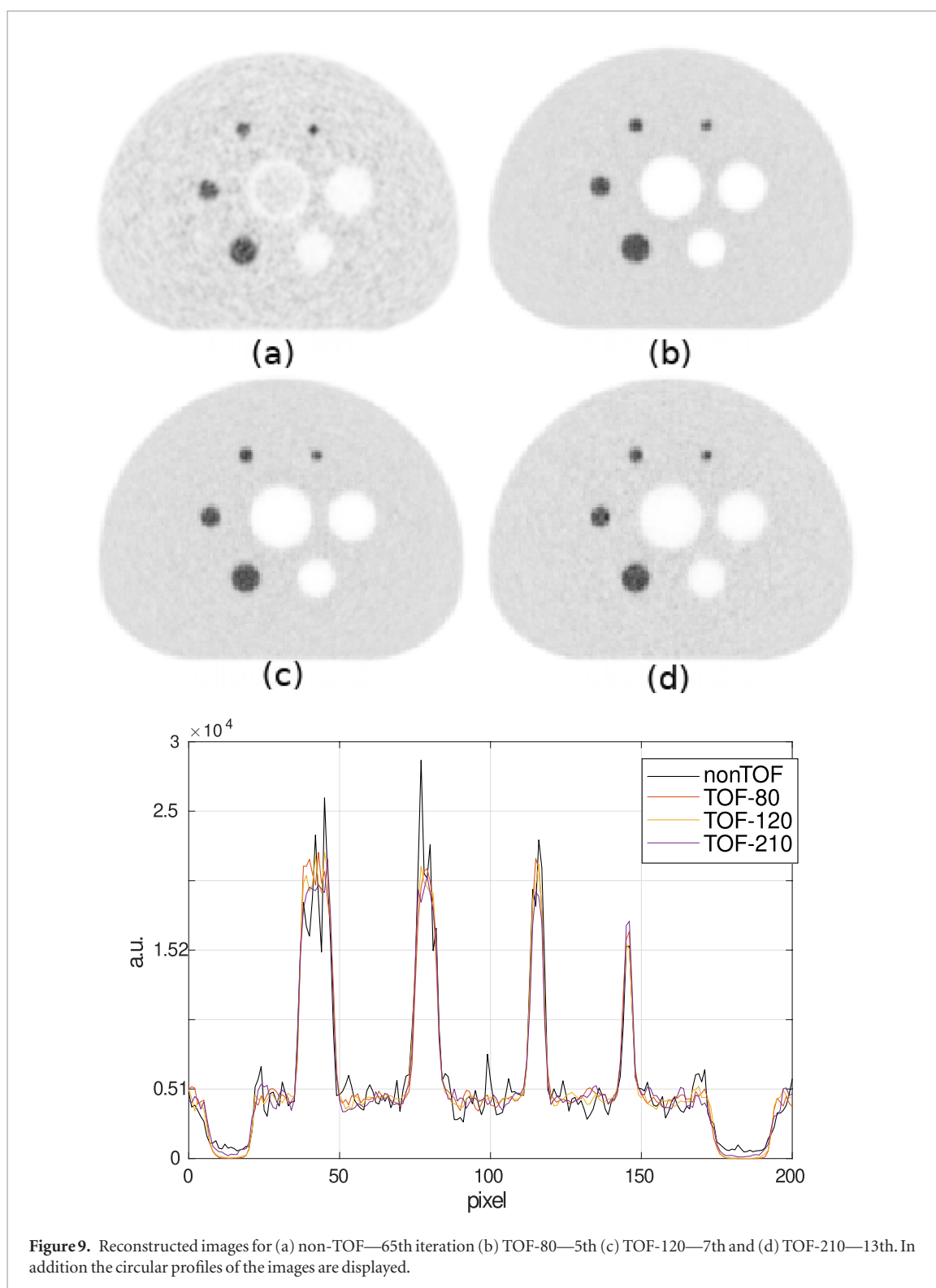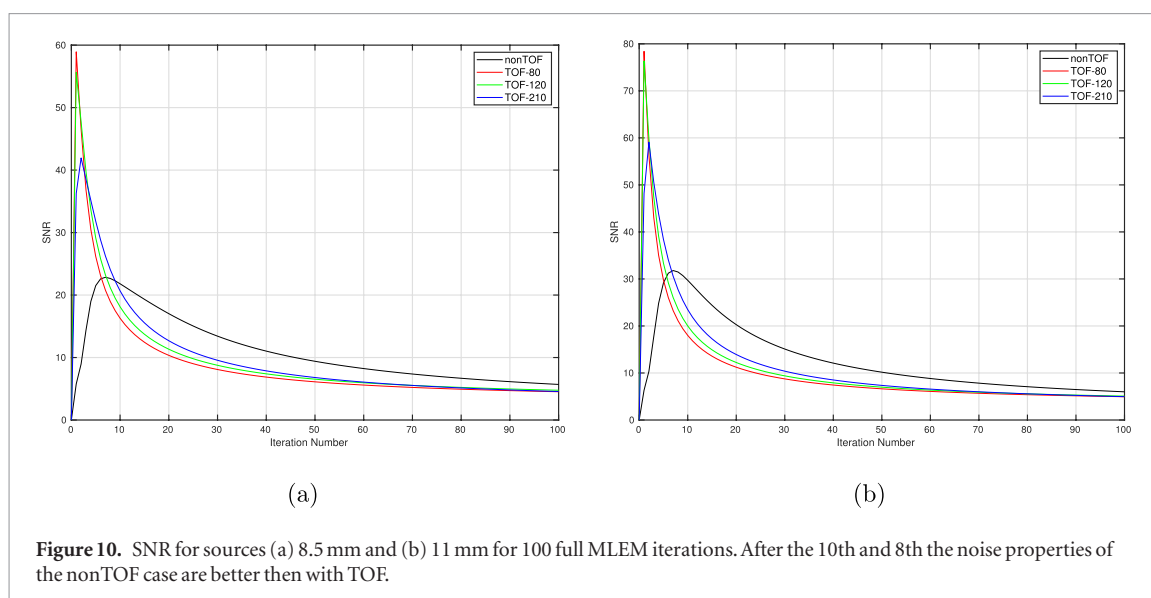
Figure 9. Reconstructed images for (a) non-TOF—65th iteration (b) TOF-80—5th (c) TOF-120—7th and (d) TOF-210—13th. In addition the circular profiles of the images are displayed.

dences or modify the resolution by a factor $\frac{l}{c}$, where l is the crystal length. To the best of our knowledge this has not been reported by other authors working with GATE simulations (Groiselle and Glick 2004, Geramifar *et al* 2008, Thoen *et al* 2013).

Results in figure 7 seem to indicate that mean ROI values do not quite match between the different TOF resolutions. Aside from convergence issues, a potential cause is the slight mismatch between the actual the photon detection time spread function and the Gaussian model used in the reconstruction (Efthimiou *et al* 2018).

The adjustment of TOF locations and mashing, which is essential for sinogram based TOF reconstruction, has a small impact on the reconstructed images, in terms of CRC and SNR. The contrast converged slightly slower, therefore more iterations are needed, which will then influence the SNR properties. However, the impact was not dramatic in the cases of TOF configurations under study.

Figure 10. SNR for sources (a) 8.5 mm and (b) 11 mm for 100 full MLEM iterations. After the 10th and 8th the noise properties of the nonTOF case are better then with TOF.

The current TOF implementation is slower than for non-TOF, as the TOF kernel modelling is applied on-the-fly on the non-TOF LOR elements. Therefore, in order to improve this trade-off in execution time, the effect of TOF-LOR truncation was investigated, in order to accelerate the reconstruction (Daube-Witherspoon *et al* 2007). It was shown that 4σ and 3σ provide most of the benefits with respect to the duration of the reconstruction without any measurable impact on the reconstructed images, in all cases tested.

In the future, we plan to implement caching of the TOF system matrix for systems with sufficient available memory. In addition, the ray-tracing algorithm will be modified to directly support TOF bins. The modification would make the algorithm to start the ray-tracing from the most probable point and move towards the integration boundaries.

Finally, our future plans also include the development of a TOF scatter simulation method (Hemmati *et al* 2017).

6. Conclusion

In this work, we presented the validation of the addition of TOF reconstruction of listmode and sinogram data in the STIR library. GATE Monte Carlo simulations were used in order to provide a well-controlled dataset for the validation. The simulated data were reconstructed using a new interface for GATE generated ROOT files. All the components presented in this paper will be distributed as open source in the next version of the STIR library.

Acknowledgments

Appendix. Effect of photon time spread on timing resolution

As presented by Gundacker *et al* (2014) and Cates and Levin (2018) at high timing resolutions the photon time spread (PTS), i.e. the uncertainty of the detection time due to photon traveling inside the crystal or optical light latency, is not negligible. In our simulation, the PTS depends only on absorption of the events at different crystal depth which introduces a source of timing uncertainty.

Under some approximations such behaviour can be described by the exponential Lambert–Beer's law (Spanoudaki and Levin 2011). Assuming that the tails of the exponential attenuation are sufficiently truncated, then the effect of PTS can be approximately modelled with a Gaussian kernel with $\mathrm{FWHM}_{\mathrm{crystal}} = \frac{l}{c}$, where l is the

length of the crystal and c is the speed of light. Thus the total timing response is given by the convolution of two distributions, and $\mathrm{FWHM}_T = \sqrt{\mathrm{FWHM_{CDR}}^2 + \mathrm{FWHM_{crystal}}^2}$, where $\mathrm{FWHM_{crystal}} = \frac{l}{c}$.

The model predicted FWHM_T of 80.1 ps, 118.2 ps and 209.36 ps, respectively, which are in agreement with the values found by fitting the simulated data.

Note that another main component of PTS is the light transfer time spread (LTTS), which is an additional factor to FWHM_T deterioration (Cates and Levin 2018) and is associated to the generation and spread of optical photons. However, this effect was not considered in our MC simulation as it would severely increase the simulation time.

ORCID iDs

Nikos Efthimiou ● https://orcid.org/0000-0003-1947-5033
Charalampos Tsoumpas ● https://orcid.org/0000-0002-4971-2477
Kris Thielemans ● https://orcid.org/0000-0002-5514-199X

References

Ahn S and Fessler J 2003 Globally convergent image reconstruction for emission tomography using relaxed ordered subsets algorithms *IEEE Trans. Med. Imaging* **22** 613–26

Ahn S, Cheng L, Shanbhag D D, Qian H, Kaushik S S, Jansen F P and Wiesinger F 2018 Joint estimation of activity and attenuation for PET using pragmatic MR-based prior: application to clinical TOF PET/MR whole-body data for FDG and non-FDG tracers *Phys. Med. Biol.* **63** 045006

Barrett H H, White T and Parra L C 1997 List-mode likelihood *J. Opt. Soc. Am.* A **14** 2914–23

Berg E and Cherry S R 2018 Using convolutional neural networks to estimate time-of-flight from PET detector waveforms *Phys. Med. Biol.* **63** 02LT01

Brunner S E and Schaart D R 2017 BGO as a hybrid scintillator/Cherenkov radiator for cost-effective time-of-flight PET *Phys. Med. Biol.* **62** 4421–39

Cates J W and Levin C S 2018 Evaluation of a clinical TOF-PET detector design that achieves 100 ps coincidence time resolution *Phys. Med. Biol.* **63** 115011

Conti M, Bendriem B, Casey M, Chen M, Kehren F, Michel C and Panin V 2005 First experimental results of time-of-flight reconstruction on an LSO PET scanner *Phys. Med. Biol.* **50** 4507–26

Conti M, Eriksson L and Westerwoudt V 2013 Estimating image quality for future generations of TOF PET scanners *IEEE Trans. Med. Imaging* **60** 87–94

Daube-Witherspoon M, Surti S, Matej S, Werner M, Jayanthi S and Karp J S 2007 Influence of time-of-flight kernel accuracy in TOF-PET reconstruction *IEEE Nuclear Science Symp. Conf. Record* vol 3 pp 1723–7

Dujardin C, Auffray E, Bourret-Courchesne E, Dorenbos P, Lecoq P, Nikl M, Vasil'ev A N, Yoshikawa A and Zhu R-Y 2018 Needs, trends, and advances in inorganic scintillators *IEEE Trans. Nucl. Sci.* **65** 1977–97

Efthimiou N, Emond E, Tsoumpas C, Thielemans K and Cawthorne C 2018 Estimation of timing resolution for very fast time-of-flight detectors in Monte Carlo simulations *IEEE Nuclear Science Symp. Conf. Record (Sydney)*

Efthimiou N, Loudos G and Panayiotakis G S 2015 Component based normalization method for rotating dual head PET scanner *J. Phys.: Conf. Ser.* **637** 012007

Erdogan H and Fessler J A 1999 Ordered subsets algorithms for transmission tomography *Phys. Med. Biol.* **44** 2835–51

Geramifar P, Ay M R, Shamsaei Zafarghandi M, Loudos G and Rahmim A 2008 Monte Carlo assessment of time-of-flight benefits on the LYSO-based discovery RX PET/CT scanner *Proc. IEEE Int. Symp. Biomedical Imaging* (https://doi.org/10.1109/ISBI.2008.4541008)

Grant A M, Deller T W, Khalighi M M, Maramraju S H, Delso G and Levin C S 2016 NEMA NU 2-2012 performance studies for the SiPM-based ToF-PET component of the GE SIGNA PET/MR system *Med. Phys.* **43** 2334–43

Green M V, Ostrow H G, Seidel J and Pomper M G 2010 Experimental evaluation of depth-of-interaction correction in a small-animal positron emission tomography scanner *Mol. Imaging* **9** 311–8

Groiselle C J and Glick S J 2004 3D PET list-mode iterative reconstruction using time-of-flight information *IEEE Symp. Conf. on Nuclear Science* vol 4 (IEEE) pp 2633–8

Gundacker S, Knapitsch A, Auffray E, Jarron P, Meyer T and Lecoq P 2014 Time resolution deterioration with increasing crystal length in a TOF-PET system *Nucl. Instrum. Methods Phys. Res.* A **737** 92–100

Hemmati H, Kamali-Asl A, Ay M and Ghafarian P 2017 Compton scatter tomography in TOF-PET *Phys. Med. Biol.* **62** 7641–58

Hubbell J and Seltzer S 1995 Tables of x-ray mass attenuation coefficients and mass energy-absorption coefficients 1 keV–20 meV for elements $z = 1$–92 and 48 additional substances of dosimetric interest *Technical Report* (Gaithersburg, MD: National Institute of Standard and Technology) PB-95-220539/XAB; NISTIR-5632 TRN: 51812148

Jacobson M *et al* 2000 Enhanced 3D PET OSEM reconstruction using inter-update Metz filtering *Phys. Med. Biol.* **45** 2417–39

Jan S *et al* 2004 GATE: a simulation toolkit for PET and SPECT *Phys. Med. Biol.* **49** 4543–61

Jin X, Chan C, Mulnix T, Liu C and Carson R E 2013 List-mode reconstruction for the Biograph mCT with probabilistic line-of-response positioning and event-by-event motion correction *Phys. Med. Biol.* **58** 5567–91

Johnson C, Thada S, Rodriguez M, Zhao Y, Iano-Fletcher A, Liow J S, Barker W C, Martino R L and Carson R E 2004 Software architecture of the MOLAR-HRRT reconstruction engine *IEEE Nuclear Science Symp. Conf. Record* vol 6 pp 3956–60

Karp J S, Surti S, Daube-Witherspoon M E and Muehllehner G 2008 Benefit of time-of-flight in PET: experimental and clinical results *J. Nucl. Med.* **49** 462–70

Kinahan P, Defrise M and Clackdoyle R 2004 Analytic image reconstruction methods *Emission Tomography: the Fundamentals of PET, SPECT* (Amsterdam: Elsevier) ch 20, pp 421–42

Kolstein M and Chmeissani M 2016 Using triple gamma coincidences with a pixelated semiconductor Compton-PET scanner: a simulation study *J. Instrum.* **11** C01039

Laval M, Moszyński M, Allemand R, Cormoreche E, Guinet P, Odru R and Vacher J 1983 Barium fluoride inorganic scintillator for subnanosecond timing *Nucl. Instrum. Methods Phys. Res.* A **206** 169–76

Martins M, Matela N, Rodrigues P, Trindade A, Oliveira N, Correia M, Cordeiro H, Ferreira N, Varela J and Almeida P 2005 Reconstruction of clear-PEM data with STIR *IEEE Nuclear Science Symp. Conf. Record* vol 4 (IEEE) pp 2098–102

Mehranian A, Kotasidis F and Zaidi H 2016 Accelerated time-of-flight (TOF) PET image reconstruction using TOF bin subsetization and TOF weighting matrix pre-computation *Phys. Med. Biol.* **61** 1309–31

Melcher C and Schweitzer J 1992 Cerium-doped lutetium oxyorthosilicate: a fast, efficient new scintillator *IEEE Trans. Nucl. Sci.* **39** 502–5

Merlin T, Stute S, Benoit D, Bert J, Carlier T, Comtat C, Filipovic M, Lamare F and Visvikis D 2018 CASToR: a generic data organization and processing code framework for multi-modal and multi-dimensional tomographic reconstruction *Phys. Med. Biol.* **63** 185005

Moses W W 2003 Time of flight in PET revisited *IEEE Trans. Nucl. Sci.* **50** 1325–30

Moses W W and Derenzo S E 1999 Prospects for time-of-flight PET using LSO scintillator *IEEE Trans. Nucl. Sci.* **46** 474–8

Moskal P *et al* 2016 Potential of the J-PET detector for studies of discrete symmetries in decays of positronium atom—a purely leptonic system *Acta Phys. Pol.* B **47** 509

Mullani N A, Ficke D C, Hartz R, Markham J and Wong G 1981 System design of fast PET scanners utilizing time-of-flight *IEEE Trans. Nucl. Sci.* **NS-28** 104–8

Mullani N A, Gaeta J, Yerian K, Wong W H, Hartz R K, Philippe E A, Bristow D and Gould K L 1984 Dynamic imaging with high resolution time-of-flight PET camera—TOFPET I *IEEE Trans. Nucl. Sci.* **31** 609–13

National Electrical Manufacturers Association 2012 *Performance Measurements of Positron Emission Tomographs* NEMA Standards Publication NU 2-2018 (Rosslyn, VA: National Electrical Manufacturers Association) (https://www.nema.org/Standards/Pages/Performance-Measurements-of-Positron-Emission-Tomographs.aspx)

Nemallapudi M V, Gundacker S, Lecoq P, Auffray E, Ferri A, Gola A and Piemonte C 2015 Sub-100 ps coincidence time resolution for positron emission tomography with LSO:Ce codoped with Ca *Phys. Med. Biol.* **60** 4635–49

Pépin A, Stute S, Jan S and Comtat C 2012 Normalization of Monte Carlo PET data using GATE *IEEE Nuclear Science Symp. Conf. Record* pp 4196–200

Popescu L M, Matej S and Lewitt R M 2004 Iterative image reconstruction using geometrically ordered subsets with list-mode data *IEEE Nuclear Science Symp. Conf. Record* vol 6 pp 3536–40

Shepp L A and Vardi Y 1982 Maximum likelihood reconstruction for emission tomography *IEEE Trans. Med. Imaging* **1** 113–22

Siddon R L 1985 Fast calculation of the exact radiological path for a three-dimensional CT array *Med. Phys.* **12** 252–5

Snyder D L 1981 A mathematical model for positron-emission tomography systems having time-of-flight measurements *IEEE Trans. Nucl. Sci.* **28** 3575–83

Snyder D L and Politte D G 1983 Image reconstruction from list-mode data in an emission tomography system having time-of-flight measurements *IEEE Trans. Nucl. Sci.* **30** 1843–9

Spanoudaki V C and Levin C S 2011 Investigating the temporal resolution limits of scintillation detection from pixellated elements: comparison between experiment and simulation *Phys. Med. Biol.* **56** 735–56

Suljic A, Tomse P, Jensterle L and Skrk D 2015 The impact of reconstruction algorithms and time of flight information on PET/CT image quality *Radiol. Oncol.* **49** 227–33

Surti S 2015 Update on time-of-flight PET imaging *J. Nucl. Med.* **56** 98–105

Surti S, Kuhn A, Werner M E, Perkins A E, Kolthammer J and Karp J S 2007 Performance of Philips Gemini TF PET/CT scanner with special consideration for its time-of-flight imaging capabilities *J. Nucl. Med.* **48** 471–80

Thielemans K, Cuplov V and Thomas B A 2015 Multi-threaded image reconstruction of 3D PET sinogram data with STIR *Fully 3D Conf.* (Newport, RI, USA)

Thielemans K, Mustafovic S and Tsoumpas C 2006 STIR: software for tomographic image reconstruction release 2 *IEEE Nuclear Science Symp. Conf. Record* vol 4 pp 2174–6

Thielemans K, Tsoumpas C, Mustafovic S, Beisel T, Aguiar P, Dikaios N and Jacobson M W 2012 STIR: software for tomographic image reconstruction release 2 *Phys. Med. Biol.* **57** 867–83

Thoen H, Keereman V, Mollet P, Van Holen R and Vandenberghe S 2013 Influence of detector pixel size, TOF resolution and DOI on image quality in MR-compatible whole-body PET *Phys. Med. Biol.* **58** 6459–79

Tomitani T 1981 Image reconstruction and noise evaluation in photon time-of-flight assisted positron emission tomography *IEEE Trans. Nucl. Sci.* **NS-28** 4581–9

Wagner R F and Brown D G 1985 Unified SNR analysis of medical imaging systems *Phys. Med. Biol.* **30** 489

Westerwoudt V, Conti M and Eriksson L 2014 Advantages of improved time resolution for TOF PET at very low statistics *IEEE Trans. Nucl. Sci.* **61** 126–33

Wong W-H, Mullani N A, Philippe E A, Hartz R and Gould K L 1983 Image improvement and design optimization of the time-of-flight *J. Nucl. Med.* **24** 52–60

Zhang Z, Rose S, Ye J, Perkins A E, Chen B, Kao C M, Sidky E Y, Tung C H and Pan X 2018 Optimization-based image reconstruction from low-count, list-mode TOF-PET data *IEEE Trans. Biomed. Eng.* **65** 936–46